PHOTONICS Research

Controllable optofluidic assembly of biological cells using an all-dielectric one-dimensional photonic crystal

Fengya Lu,[1] Lei Gong,[1,2,4] Yan Kuai,[1] Xi Tang,[1] Yifeng Xiang,[3] Pei Wang,[1] and Douguo Zhang[1,2,5]

[1]Advanced Laser Technology Laboratory of Anhui Province, Department of Optics and Optical Engineering, University of Science and Technology of China, Hefei 230026, China
[2]Hefei National Laboratory for Physical Sciences at the Microscale, University of Science and Technology of China, Hefei 230026, China
[3]Fujian Provincial Key Laboratory of Photonics Technology, College of Photonic and Electronic Engineering, Fujian Normal University, Fuzhou 350117, China
[4]e-mail: leigong@ustc.edu.cn
[5]e-mail: dgzhang@ustc.edu.cn

Received 6 August 2021; revised 21 October 2021; accepted 25 October 2021; posted 28 October 2021 (Doc. ID 439288); published 9 December 2021

Opto-thermophoretic manipulation is emerging as an effective way for versatile trapping, guiding, and assembly of biological nanoparticles and cells. Here we report a new opto-thermophoretic tweezer based on an all-dielectric one-dimensional photonic crystal (1DPC) for reversible assembly of biological cells with a controllable center. To reveal its ability of long-range optofluidic manipulation, we demonstrate the reversible assembly of many yeast cells as well as *E. coli* cells that are dispersed in water solution. The 1DPC-based tweezer can also exert short-range optical gradient forces associated with focused Bloch surface waves excited on the 1DPC, which can optically trap single particles. By combining both the optical and thermophoretic manipulation, the optically trapped single polystyrene particle can work as a controllable origin of the reversible cellular assembly. Numerical simulations are performed to calculate the temperature distribution and convective flow velocity on the 1DPC, which are consistent with the experimental observations and theoretically confirm the long-range manipulations on the all-dielectric 1DPC platform. The opto-thermophoretic tweezers based on all-dielectric 1DPC endow the micromanipulation toolbox for potential applications in biomedical sciences.

https://doi.org/10.1364/PRJ.439288

1. INTRODUCTION

Manipulating biological cells and nanoparticles is of paramount importance in biomedical studies such as cell interaction, cell adhesion, cell rheology, metastasis of circulating tumor cells, single cell transfection, and tissue engineering [1–4]. Optical tweezers have proven to be a powerful tool for trapping and manipulating biological particles [5–9]. However, conventional optical tweezers trap tiny objects using optical gradient forces near a tightly focused laser beam [10–12], which has a limitation in long-range transportation and manipulation of target objects and cannot manipulate many biological objects [13]. Various types of novel tweezers have been developed to address this limitation of conventional optical tweezers [14,15]. For example, a strategy of combining the advantages of optical and plasmonic tweezers is proposed to achieve dynamic manipulation and long-range delivery of target objects [16–19]. Electrothermoplasmonic tweezers can transport particles over a long distance and trap them at the plasmonic structures [13,20,21]. Recently, opto-thermophoretic tweezers have emerged as powerful tools for long-range optical manipulation [22–24]. Opto-thermophoretic manipulation exploits the thermophoretic migration of particles and colloidal species under a light-controlled temperature gradient field [25–27]. The thermophoretic pumping forces of opto-thermophoretic tweezers are beyond the action range of direct optical gradient forces, allowing long-range manipulation. Thus, opto-thermophoretic manipulation provides an effective strategy for assembly of many cells. Active assembly of cells could help gain insights in tissue development and diseases [28–30], which always involves manipulation of many cells [31].

In this paper, we demonstrate a new opto-thermophoretic tweezer based on an all-dielectric one-dimensional photonic crystal (1DPC) platform for controllable assembly of many biological cells. Different from the metallic substrates adopted in conventional thermophoretic tweezers, the all-dielectric 1DPC can provide a stronger temperature gradient for thermophoretic manipulation due to the excitation of the Bloch surface waves (BSWs). BSWs are electromagnetic surface waves excited at the

interface between a truncated periodic dielectric multilayer with a photonic band gap (PBG) and its surrounding medium [32,33]. Until now, BSWs have been applied in nanoscale optical circuits [34,35], fluorescence emission enhancement or sorting [36], enhanced Goos–Hanchen shift [37], and strong polariton-polariton nonlinearities of 2D materials [38]. However, to the best of our knowledge, there is no report on how to use the thermal and optical forces induced by the BSWs of 1DPC to trap and assemble many biological cells. The proposed opto-thermophoretic tweezer allows reversible assembly of biological cells by the thermophoresis and long-ranged optofluidic pumping force, due to the excitation of the BSWs on the 1DPC. Focused BSWs also allow us to stably trap a single particle by the short-ranged optical gradient force, which can serve as the initial origin for the reversible cellular assembly. Then the proposed thermophoretic tweezer can take the advantages of both optical and thermophoretic manipulation simultaneously.

2. METHODS AND EXPERIMENTS

A. Structure of 1DPC and Its Property

The opto-thermophoretic tweezer is constructed based on an all-dielectric 1DPC. The sketch of the 1DPC geometry is illustrated in Fig. 1(a), which is a dielectric multilayer nanostructure with a well-designed PBG. The dielectric multilayer is composed of Si_3N_4 with high refractive index ($n = 2.14 + i \times 10^{-3}$) and SiO_2 with low refractive index ($n = 1.47 + i \times 10^{-5}$) alternately. The thickness of Si_3N_4 layer is 132 nm, the SiO_2 layer is 145 nm, the top Si_3N_4 layer is 37 nm, and there are seven layers in total. The calculated reflectance spectrum for such a 1DPC at a wavelength of 671 nm is shown in Fig. 1(b). The dip for transverse-electric (TE)-polarized

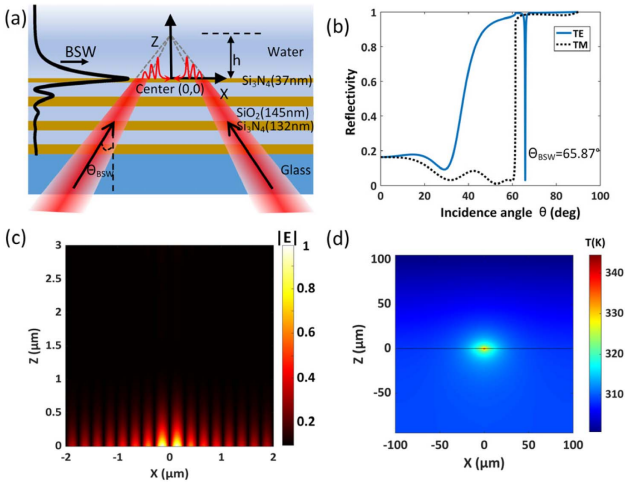

Fig. 1. Schematic of the 1DPC and its property. (a) Schematic diagram of the 1DPC. $z = 0$ is the 1DPC–water interface, and the point (0,0) represents the center of the focused beam. The laser beam is focused above the 1DPC–water interface at distance of h. (b) Calculated angular reflectance spectra of the 1DPC for TE- (blue) and TM- (black) polarized incident beams. (c) The electric field distribution of the focused BSWs in the x–z plane normalized by the maximum. (d) Simulated temperature distribution in the x–z plane. The horizontal line at $z = 0$ indicates the 1DPC–water interface.

radiation at $\theta = 65.87°$ corresponds to the BSWs' excitation, which has a narrow resonance width. Besides, at larger incident angles, the incident beam is almost totally reflected (reflectivity ≈ 1), so the intensity of incident beam is negligible compared to the BSWs. To achieve a high excitation efficiency with an oil-immersed objective, a ring-shaped laser beam with an azimuthal polarization at the wavelength of 671 nm is focused above the 1DPC–water interface, the defocused height is set to be 5 μm, and the incident angle of the laser beam is tuned to the excitation angle of the BSW mode. The excited BSW is localized near the 1DPC–water interface, which exponentially decays into water and propagates horizontally toward the center from all azimuthal directions. The interference field of excited BSWs forms a virtual optical probe at the center of the surface as shown in Fig. 1(c). This process is similar to the excitation of highly focused plasmonic field on a flat metal film [39,40].

Due to the absorption characteristics and low thermal conductivity of the dielectric multilayer, the virtual optical probe will induce a localized spot heat source at the water–1DPC interface. A stable-state temperature distribution can be obtained when the heat diffusion between the heated 1DPC and the water environment achieves a balance. Quantitatively, we simulated the temperature distribution of the region near the interface by using the finite element method (FEM) [41]. The thickness of the water film is set to be 200 μm, and the initial temperature of the surrounding environment is set to be 293.15 K. The laser power is 60 mW, and the defocused height is set to be 5 μm above the 1DPC–water interface. All these parameters are consistent with the experimental ones that will be detailed below. Figure 1(d) presents the calculated temperature profiles on the incident x–z plane, where $z = 0$ nm indicates the 1DPC–water interface. The Au film substrate is commonly adopted in traditional thermophoretic tweezers [22,42]. Compared with it, the 1DPC substrate can achieve lower temperatures but comparable temperature gradients due to the low thermal conductivity of the all-dielectric 1DPC. It should be noted that the thermophoretic force is dependent on the temperature gradient rather than the absolute temperature value.

B. Principle of Optofluidic Assembly of Biological Cells

Opto-thermophoretic tweezers manipulate particles by a laser-generated temperature gradient field in the fluids. The thermal gradient drives the particles to move toward the cold or the hot regions. This phenomenon is termed as thermophoresis or the Soret effect, and the driving force is thus called as the thermophoretic force [42,43]. Theoretically, the drift velocity of objects is linear with the temperature gradient ∇T, which reads

$$v = -D_T \nabla T, \tag{1}$$

where D_T is the thermophoretic mobility. $D_T = S_T D$, where S_T is the Soret coefficient and D is the diffusion coefficient. Generally, the S_T decides the direction of the thermal diffusion: when $S_T > 0$, particles move to cold regions; while $S_T < 0$, particles move toward hot regions [24]. In practice, the thermal gradient induced particle motion is related to many factors, such as interfacial properties, temperature, salinity, particle-particle interaction, and solvent compositions. Here we are trying

to trap and assemble biological cells, and the interfacial interaction between the cell membrane and the water molecules plays a critical role in this situation. Most of the biological cells have negative surface charge because of the phospholipid bilayer in cell membrane. Then orientated water molecules form on the electric double layers of the cell membrane under the electric field as shown in Fig. 2(a). This structure results in a negative Soret coefficient, and thus cells migrate from cold to hot regions. That means the direction of drift velocity is consistent with the temperature gradient. However, it is difficult to get the exact value of the Soret coefficient, so calculation of the thermophoretic force on biological cells is a challenging problem.

Considering the thermophilic nature of biological cells, we further analyze the optofluidic force for cells under the temperature field. For this purpose, the temperature gradient is calculated based on the temperature field of the 1DPC in Fig. 1(d). Figure 2(b) shows the calculated temperature gradient distributions along radial (∇T_r) and vertical (∇T_z) directions in the x–y plane for our 1DPC substrate. The maximum temperature gradients of $\nabla T_z = -3.2 \times 10^7$ K/m and $\nabla T_r = -1.3 \times 10^6$ K/m were created. The negative sign indicates that the temperature gradient points toward the coordinate origin. Under such a thermal field, the biological cells with negative Soret coefficients will move to the hot regions and finally be trapped at the hot spot. In fact, apart from the thermophoresis, the temperature field also generates a fluidic flow. Figure 2(c) depicts the simulated flow streamlines above the interface by the FEM [41], where the arrows indicate the flow direction of the water. The hydrodynamic counterflow in the fluid moves radially inward along the surface, but then flows upward normal to the interface. The color map is the amplitude of the speed of flow in the water phase. The long-ranged and attractive character of the flow entrains suspended cells and draws them toward the focus. Under the action of both the thermophoresis and flow-induced pumping force, cells can finally closely aggregate.

Furthermore, the all-dielectric 1DPC substrate can be adopted to generate focused BSWs, which can stably trap a single particle due to the short-ranged optical gradient force [18]. In this manner, our proposed scheme allows combining the advantages of optical and thermophoretic manipulation. For instance, the optical force of focused BSWs could capture a single particle to serve as a controllable origin of the assembly. Thus, the 1DPC-based tweezers enable versatile trapping and manipulation by long-ranged and short-ranged forces simultaneously. For the cellular assembly, a schematic diagram that illustrates the main actions in the optofluidic manipulation is presented in Fig. 2(d), including the flow-induced force (arrows in yellow), the optical force associated with the focused BSWs (illustrated by a focused beam), and thermophoresis (arrows in red) caused by temperature gradient.

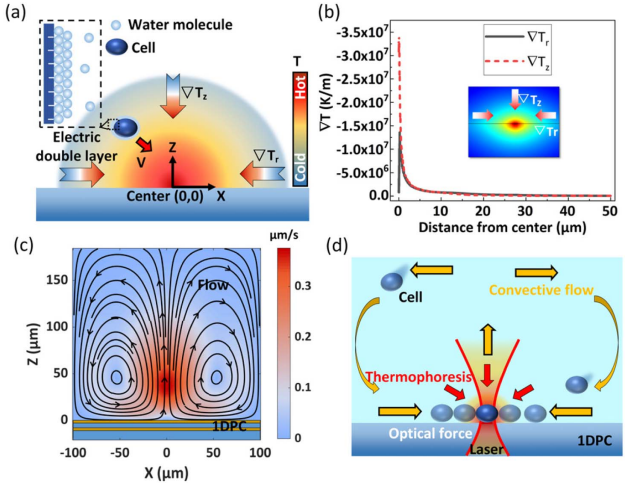

Fig. 2. Working principle of cell assembly with the optofluidic manipulation. (a) Thermophoretic trapping of biological cells in fluidics. Water molecules form an electric double layer on the surface of the negatively charged cells. Under the action of thermophoresis, the biological cells with negative Soret coefficients will move to the hot regions and finally be trapped at the hot spot. The red arrow indicates the movement direction of cells. (b) Simulated maps of temperature gradient along the radial (∇T_r, black solid line) and vertical directions (∇T_z, red dotted line) in the x–y plane, where the plane is located at 100 nm above the 1DPC–water interface. The inset shows the direction of temperature gradient. (c) The simulated convective velocity distribution inside the water. The color map shows the magnitude of the flow speed, and the streamlines represent the directions of the flow. (d) Main actions in the optofluidic assembly of biological cells: the flow-induced force (arrows in yellow), the thermophoresis (arrows in red) caused by temperature gradient, and the optical force (illustrated by a focused laser beam) associated with the focused BSWs.

C. Experimental Setup of the Opto-Thermophoretic Tweezer

The opto-thermophoretic tweezer is constructed based on an inverted microscope, which contains a BSW excitation scheme and the 1DPC sample as shown in Fig. 3. A laser with an emission power of 60 mW working at the wavelength of 671 nm serves as the excitation source. The polarization of BSW is TE for our 1DPC structure. To improve the excitation efficiency, a ring-shaped laser beam generated by a pair of axicons is adopted. The shaped laser beam passes through a linear polarizer and a vortex retarder to generate an azimuthally polarized beam. An oil immersion objective (numerical aperture,

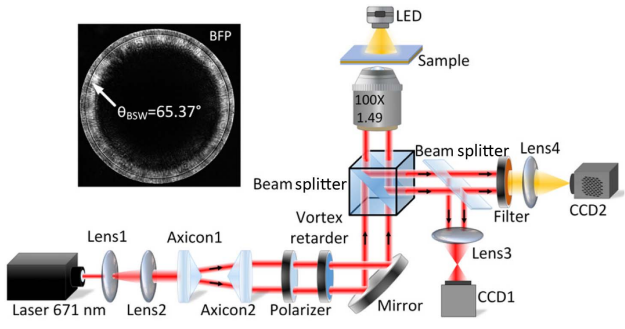

Fig. 3. Schematic diagram of the experimental setup. The pair of axicons can generate a ring-shaped laser beam; besides, the polarizer and vertex retarder are used to generate an annular azimuthally polarized beam. The inset graph shows the BFP image of the laser beam reflected from the 1DPC shot by CCD1, in which the dark ring (labeled $\theta_{BSW} = 65.37°$) verifies that the BSW has been efficiently excited in all directions by the ring-shaped azimuthally polarized beam.

NA = 1.49, 100×) tightly focuses the beam onto the 1DPC substrate to excite BSWs. The defocus height is set to be 5 μm over the water–1DPC interface, which is controlled by a piezoelectric stage with nanometer accuracy. An imaging configuration consisting of Lens3 and CCD1 is used to observe the profile of the laser beam at the back focal plane (BFP). As shown in the inset, the sharp dark ring verifies that the BSWs have been efficiently excited in all directions by the ring-shaped azimuthally polarized beam with the diameter of ∼22 μm on the sample. According to the NA, the angle of the BSW can be derived to be $\theta_{BSW} = 65.37°$, which is consistent with theoretical calculation [Fig. 1(b)]. Above the 1DPC substrate, the suspended cells in the fluids can be trapped and assembled with the tweezer. CCD2 together with Lens4 and a short-pass filter is adopted to record the manipulation process under the illumination of an LED.

3. RESULTS AND DISCUSSIONS

A. Optical and Thermophoretic Manipulation

To prove the ability of our 1DPC-based opto-thermophoretic tweezer, we performed a set of experiments to demonstrate the optical and thermophoretic manipulation. We first demonstrate the long-ranged and attractive character of the flow-induced pumping force. For this purpose, 5 μm polystyrene (PS) beads are dispersed in water, and their movements are recorded after the laser is turned on. Figure 4(a) shows some frames of their behavior, and Visualization 1 presents the whole process. The PS particles in the whole field of view move along the surface toward the focus ($t = 10$ s), but then they are pushed away from the surface ($t = 15$ s and 20 s). It is obvious that the optical force cannot play a role at such a long distance.

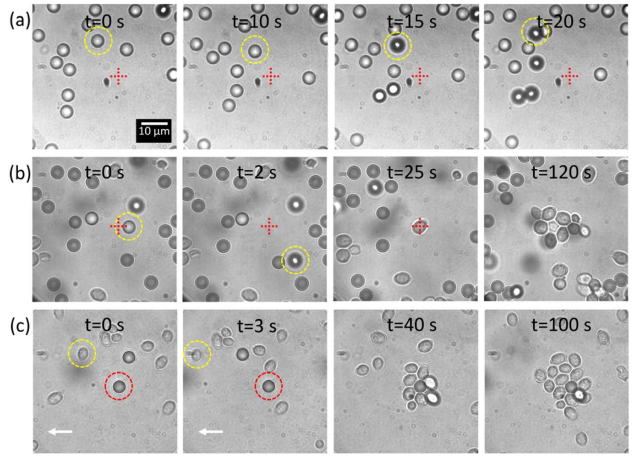

Fig. 4. Optical and thermophoretic manipulation of colloid particles and yeast cells. (a) The uncaptured particles (yellow circle) are convected away from the interface by the optofluidic flow. (b) In contrast to the colloid particles (yellow circle), yeast cells are trapped ($t = 25$ s) and finally form an assembly on the surface. (c) A single colloid particle (shown in red circle) is trapped by the short-ranged optical force and transported to any position, where the white arrow indicates the movement direction and the uncaptured yeast cell was labeled with a yellow circle. When the substrate stops, the cells gather around the trapped particle under the action of the thermal convection flow and thermophoresis. Scale bar: 10 μm.

This phenomenon is consistent with the counterflow pattern in Fig. 2(c).

In addition, we investigated the role of the thermophoresis using a mixed solution of PS particles and yeast cells. The result is shown in Fig. 4(b). As expected, both the PS beads and the yeast cells are pumped toward the center by thermal convection flow, but then they show totally different behaviors near the focus. The PS beads (yellow circle) are pushed away from the surface, while the yeast cells are trapped ($t = 25$ s), and more and more cells aggregate and finally form a self-assembly ($t = 120$ s). More details can be seen in Visualization 2. In fact, the different behaviors are attributed to two reasons: (1) the larger scattering force attributed to the refractive index mismatch for the colloid; (2) the different thermophoresis responses of the colloids and cells. The Soret coefficient is positive for the colloids when they do not have surface ligands and the solvent is deionized water, but it is negative for the cells due to the negative surface charge. To verify it, we measured the surface charge of the yeast cells and got a zeta potential of −28.2 mV. Besides, the thermophoresis forces on the yeast cells overcome the pushing-away force of the convection flow. As a result, the PS particles were guided upward, while the yeast cells were not pushed upward but remained at the interface as we observed in Fig. 4(b).

Finally, we analyzed the function of the optical gradient forces in the manipulation. In the above experiments, we find that once a particle migrates toward the focus, the short-ranged optical gradient force associated with the focused BSWs can trap it. Different from the thermophoresis force, the optical gradient force could trap both the yeast cell and the PS bead. Even if we moved the substrate quickly, the particle could be stably trapped. As shown in Fig. 4(c), the trapped particle (red circle) does not move with the substrate, but the uncaptured yeast cells (labelled by yellow circles) do. Once the substrate stops, the yeast cells assemble around the trapped particle immediately under the action of the thermal convection flow and thermophoresis. The whole manipulation process is shown in Visualization 3. In this process, the optical gradient force enables trapping a single particle as the hot spot of the active cellular assembly and moving it to any position on the surface of 1DPC.

B. Reversible Assembly of Yeast Cells

By exploiting the ability of optical and thermophoretic manipulation, we achieve controllable assembly of many yeast cells. Figure 5(a) shows the crystallization process of the trapped yeast cells. Without the laser illumination ($t = 0$ s), the cells diffused freely. Once the laser was switched on, a single yeast cell was trapped by the optical force immediately, and the surrounding diffused cells were pumped toward the trapped one, leading to a rapid assembly within a few seconds (∼5 s). As time went, more and more cells aggregated and formed a tightly packed assembly around the beam center (Visualization 4). Note that the cells were driven from positions out of the range of the laser beam or even outside the field of view, suggesting a long-ranged delivery. Further, once the laser was turned off, the crystallization returned to a state of free diffusion ($t = 180$ s), which proves that the assembly was induced by the optofluidic effect. During the process, we

observed that the yeast cells packed quickly near the focus but slowly at the periphery. Quantitatively, we measured the averaged migration velocity at different radial distances. The velocity versus distance curve is shown in Fig. 5(b), where each point was calculated by averaging velocities in randomly selected directions. The migration velocity of the cells out of the range of 20 μm is about 0.4 μm/s, basically consistent with the simulated convection velocity in Fig. 2(c). The velocities increase significantly as the cells get closer to the center, up to 3 μm/s. Clearly, the convection flow is not able to transport cells up to such a high velocity. It is the thermophoresis force and short-ranged optical force that play the role.

To further characterize the cellular assembly, we analyzed the number of trapped cells as a function of illumination time. As depicted in Fig. 5(c), the number of trapped cells increases exponentially at the beginning and becomes saturated finally. If the illumination time is long enough, the yeast cells throughout the entire field of view can form a crystallization as shown in Fig. 6(a). Due to the yeast cells being deformable and not uniform in size, at the central region, the soft cells are deformed in response to the surrounding stresses, distinguished from the point to point contact among rigid spheres [44]. The mechanical forces were transmitted among individual cells via cell–cell contact, and thus the cells were squeezed into polygon crystallization. Besides, this shape deformation might be involved in cell–cell adhesions. Figure 6(b) shows the outlines of the deformed cells. It is noted that the edge number of the polygon

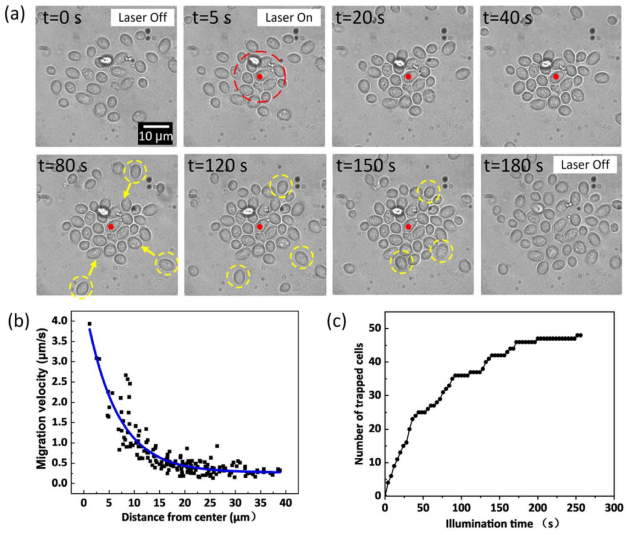

Fig. 5. Reversible assembly of yeast cells. (a) Time-sequenced set of the cell assembly under the irradiation of 60 mW laser power at 671 nm. At $t = 5$ s, the laser is switched on, and a single yeast cell is trapped (red dot). Other yeast cells move to the center and form a tightly packed assembly under the action of the thermophoresis and long-ranged thermal convection. The yeast cells labeled with yellow circles gather from different directions. Once the laser is switched off ($t = 180$ s), the cells return to a state of free diffusion. The red dotted circle indicates the illumination area of the laser beam. (b) The migration velocity of cells as a function of the distance from the center, where the solid blue line fitted by polynomials is drawn as a visual guide. (c) The number of trapped cells as a function of the illumination time. The scale bar is 10 μm.

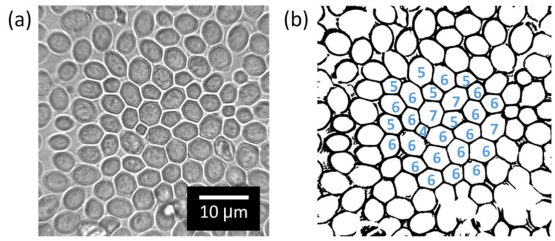

Fig. 6. Crystallization of yeast cells. (a) Image of the optofluidic crystallization of yeast cells. The cells are squeezed into polygons due to their deformability. The scale bar is 10 μm. (b) Outlines of the deformed cells. The edge numbers of the polygons are labeled.

varies with the size of the cell, ranging from 4 to 8. This kind of cell crystallization is similar to the real morphology of tissues, such as epithelial tissue [29,30]. Thus, our method provides a way to mimic the structure in tissues.

To verify that the optothermal assembly relies on the excitation of the BSWs, we tested the assembly using excited laser beam with different angles of incidence. Figure 7(a) illustrates the setup with a single-direction illumination [45], where the BSWs were excited by a laser beam with TE polarization on the 1DPC at a given angle of incidence. First, we set the angle of incidence fixed at θ_{BSW}. The yeast cells aggregated quickly and formed a tightly packed assembly in several minutes as demonstrated in Fig. 7(b). By contrast, if the incidence angle was decreased or increased, the yeast cells could not assemble any more as shown in Figs. 7(c) and 7(d). The results directly demonstrate that the BSWs play a critical role in the assembly of cells.

C. Trapping and Assembly of *E. coli* Cells

Apart from the yeast cells, we tried to trap and assemble the *Escherichia coli* (*E. coli*) cells, demonstrating the universality of the proposed approach in manipulating live cells. Compared with yeast cells, *E. coli* cells have a relatively low refractive index and small size, ~700 nm in width and 2 μm in length. *E. coli* cells are peritrichously flagellated bacteria and are active particles. They swim in a random and disorder pattern, making it difficult to trap and assemble *E. coli*. Here we show that our

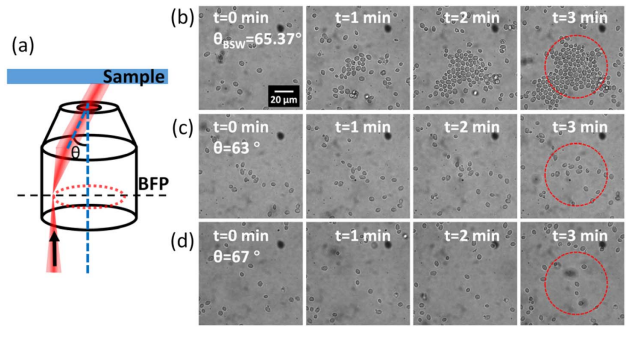

Fig. 7. Angular dependence of the cell assembly. (a) Schematic of the incident angle. (b) Assembly process of yeast cells at θ_{BSW} (65.37°). (c), (d) No accumulation of yeast cells forms after 4 min when the incidence angle mismatches θ_{BSW}. The dashed circles indicate the illumination region of the laser beam. Scale bar: 20 μm.

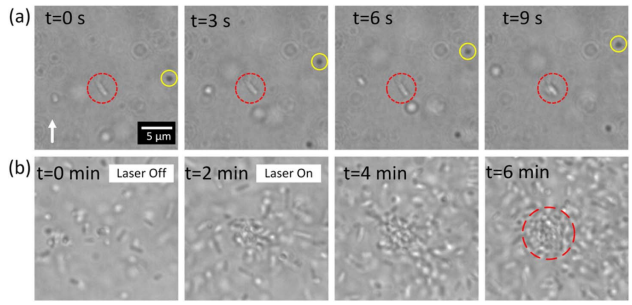

Fig. 8. Trapping and assembly of *E. coli* cells. (a) Stable trapping of a single *E. coli* (red circle). The white arrow indicates the direction of stage movement, and the yellow circle indicates the reference on the substrate. (b) Assembly process of *E. coli*. The scale bar is 5 μm.

1DPC-based opto-thermophoretic tweezer can achieve the manipulation. As demonstrated in Fig. 8(a), the *E. coli* could be stably trapped even under the pulling of the flow. In addition, under the action of the thermal convection and thermophoresis, the free-swimming *E. coli* cells aggregated and finally formed an assembly. Visualization 5 and Fig. 8(b) show the process of the assembly, where the concentration of the bacteria at the central region is significantly higher than that at the surrounding area.

4. CONCLUSIONS

We have proposed a new opto-thermophoretic tweezer based on an all-dielectric 1DPC and applied it for controllable assembly of biological cells. Different from the metallic substrates used in conventional opto-thermophoretic tweezers, the all-dielectric 1DPC provides lower temperatures but higher temperature gradients in the fluids, which is beneficial for low-power optofluidic manipulation. This all-dielectric 1DPC is much more stable than the metallic thin film and can be used for many times in experiments. It is well known in cell biology that the techniques used to culture cells on dielectric substrates are more mature and generally applicable than those for growth on metal films. The 1DPC-based tweezer enables the combination of the long-ranged flow-induced force, local thermophoresis force and short-ranged optical force that is associated with focused BSWs. By exploiting the capacity of both optical and thermophoretic manipulation, we demonstrated controllable assembly of many yeast cells as well as *E. coli* cells. In addition, numerical simulations were performed to calculate the temperature distribution and convective flow velocity, which are consistent with the experimental observations and then further justify the feasibility of the proposed method. The optofluidic manipulation with the all-dielectric 1DPC platform opens a new way for long-range transportation, sorting, and self-assembly of biological cells, promoting potential applications in biomedical sciences, such as biofilm development, quorum sensing, and antimicrobial resistance [46]. Besides, the high sensitivity of the BSWs to their environments will benefit real-time monitoring of the physical or chemical changes of the trapped and assembled biological cells [47–49].

Funding. National Natural Science Foundation of China (12134013, 11774330, U20A20216, 31870759, 11974333, 61535011, 62105066); Advanced Laser Technology Laboratory of Anhui Province (20192301); Key Research Development Program of Anhui Province (202104a05020010); Hefei Municipal Natural Science Foundation (2021007); The Anhui Initiative in Quantum Information Technologies (AHY090000); Natural Science Foundation of Fujian Province (2021J01163).

Acknowledgment. D. Zhang is supported by a USTC Tang Scholarship. We acknowledge support from the University of Science and Technology of China's Center for Micro and Nanoscale Research and Fabrication.

Disclosures. The authors declare no competing financial interests.

Data Availability. Data underlying the results presented in this paper are not publicly available at this time but may be obtained from the authors upon reasonable request.

REFERENCES

1. P. Jing, Y. Liu, E. G. Keeler, N. M. Cruz, B. S. Freedman, and L. Y. Lin, "Optical tweezers system for live stem cell organization at the single-cell level," Biomed. Opt. Express **9**, 771–779 (2018).
2. M. Waleed, S. U. Hwang, J. D. Kim, I. Shabbir, S. M. Shin, and Y. G. Lee, "Single-cell optoporation and transfection using femtosecond laser and optical tweezers," Biomed. Opt. Express **4**, 1533–1547 (2013).
3. K. Berghoff, W. Gross, M. Eisentraut, and H. Kress, "Using blinking optical tweezers to study cell rheology during initial cell-particle contact," Biophys. J. **120**, 3527–3537 (2021).
4. V. M. Freitas, G. Hilfenhaus, and M. L. Iruela-Arispe, "Metastasis of circulating tumor cells: speed matters," Dev. Cell **45**, 3–5 (2018).
5. Q. Zhao, H. W. Wang, P. P. Yu, S. H. Zhang, J. H. Zhou, Y. M. Li, and L. Gong, "Trapping and manipulation of single cells in crowded environments," Front Bioeng. Biotechnol. **8**, 422 (2020).
6. A. Ashkin, J. M. Dziedzic, and T. Yamane, "Optical trapping and manipulation of single cells using infrared-laser beams," Nature **330**, 769–771 (1987).
7. A. H. J. Yang, S. D. Moore, B. S. Schmidt, M. Klug, M. Lipson, and D. Erickson, "Optical manipulation of nanoparticles and biomolecules in sub-wavelength slot waveguides," Nature **457**, 71–75 (2009).
8. M. C. Zhong, X. B. Wei, J. H. Zhou, Z. Q. Wang, and Y. M. Li, "Trapping red blood cells in living animals using optical tweezers," Nat. Commun. **4**, 1768 (2013).
9. M. C. Zhong, L. Gong, J. H. Zhou, Z. Q. Wang, and Y. M. Li, "Optical trapping of red blood cells in living animals with a water immersion objective," Opt. Lett. **38**, 5134–5137 (2013).
10. A. Ashkin, J. M. Dziedzic, J. E. Bjorkholm, and S. Chu, "Observation of a single-beam gradient force optical trap for dielectric particles," Opt. Lett. **11**, 288–290 (1986).
11. D. G. Grier, "A revolution in optical manipulation," Nature **424**, 810–816 (2003).
12. Y. J. Yang, Y. X. Ren, M. Z. Chen, Y. Arita, and C. Rosales-Guzman, "Optical trapping with structured light: a review," Adv. Photon. **3**, 034001 (2021).
13. J. C. Ndukaife, A. V. Kildishev, A. G. Nnanna, V. M. Shalaev, S. T. Wereley, and A. Boltasseva, "Long-range and rapid transport of individual nano-objects by a hybrid electrothermoplasmonic nanotweezer," Nat. Nanotechnol. **11**, 53–59 (2016).
14. V. Sharma, D. Paul, S. K. Chaubey, S. Tiwari, and G. V. P. Kumar, "Large-scale optothermal assembly of colloids mediated by a gold microplate," J. Phys. Condens. Matter **32**, 324002 (2020).

15. P. P. Patra, R. Chikkaraddy, R. P. N. Tripathi, A. Dasgupta, and G. V. P. Kumar, "Plasmofluidic single-molecule surface-enhanced Raman scattering from dynamic assembly of plasmonic nanoparticles," Nat. Commun. **5**, 4357 (2014).
16. W. Ding, T. Zhu, L.-M. Zhou, and C.-W. Qiu, "Photonic tractor beams: a review," Adv. Photon. **1**, 024001 (2019).
17. Y. Q. Zhang, X. J. Dou, Y. M. Dai, X. Y. Wang, C. J. Min, and X. C. Yuan, "All-optical manipulation of micrometer-sized metallic particles," Photon. Res. **6**, 66–71 (2018).
18. Y. Zhang, C. Min, X. Dou, X. Wang, H. P. Urbach, M. G. Somekh, and X. Yuan, "Plasmonic tweezers: for nanoscale optical trapping and beyond," Light Sci. Appl. **10**, 59 (2021).
19. M. L. Juan, M. Righini, and R. Quidant, "Plasmon nano-optical tweezers," Nat. Photonics **5**, 349–356 (2011).
20. Z.-S. Li, T.-W. Lu, P.-R. Huang, and P.-T. Lee, "Efficient nano-tweezers via a silver plasmonic bowtie notch with curved grooves," Photon. Res. **9**, 281–288 (2021).
21. C. Hong, S. Yang, and J. C. Ndukaife, "Stand-off trapping and manipulation of sub-10 nm objects and biomolecules using opto-thermo-electrohydrodynamic tweezers," Nat. Nanotechnol. **15**, 908–913 (2020).
22. L. Lin, X. Peng, X. Wei, Z. Mao, C. Xie, and Y. Zheng, "Thermophoretic tweezers for low-power and versatile manipulation of biological cells," ACS Nano **11**, 3147–3154 (2017).
23. D. Niether and S. Wiegand, "Thermophoresis of biological and biocompatible compounds in aqueous solution," J. Phys. Condens. Matter **31**, 503003 (2019).
24. S. Liu, L. Lin, and H. B. Sun, "Opto-thermophoretic manipulation," ACS Nano **15**, 5925–5943 (2021).
25. M. Braun, A. P. Bregulla, K. Gunther, M. Mertig, and F. Cichos, "Single molecules trapped by dynamic inhomogeneous temperature fields," Nano Lett. **15**, 5499–5505 (2015).
26. M. Braun and F. Cichos, "Optically controlled thermophoretic trapping of single nano-objects," ACS Nano **7**, 11200–11208 (2013).
27. F. M. Weinert and D. Braun, "Observation of slip flow in thermophoresis," Phys. Rev. Lett. **101**, 168301 (2008).
28. J. A. Park, L. Atia, J. A. Mitchel, J. J. Fredberg, and J. P. Butler, "Collective migration and cell jamming in asthma, cancer and development," J. Cell Sci. **129**, 3375–3383 (2016).
29. C. P. Heisenberg and Y. Bellaiche, "Forces in tissue morphogenesis and patterning," Cell **153**, 948–962 (2013).
30. C. Guillot and T. Lecuit, "Mechanics of epithelial tissue homeostasis and morphogenesis," Science **340**, 1185–1189 (2013).
31. G. Makey, S. Galioglu, R. Ghaffari, E. D. Engin, G. Yıldırım, Ö. Yavuz, O. Bektaş, Ü. S. Nizam, Ö. Akbulut, Ö. Şahin, K. Güngör, D. Dede, H. V. Demir, F. Ö. Ilday, and S. Ilday, "Universality of dissipative self-assembly from quantum dots to human cells," Nat. Phys. **16**, 795–801 (2020).
32. P. Yeh, A. Yariv, and C. S. Hong, "Electromagnetic propagation in periodic stratified media. 1. General theory," J. Opt. Soc. Am. **67**, 423–438 (1977).
33. L. Yu, E. Barakat, T. Sfez, L. Hvozdara, J. Di Francesco, and H. P. Herzig, "Manipulating Bloch surface waves in 2D: a platform concept-based flat lens," Light Sci. Appl. **3**, e124 (2014).
34. E. Descrovi, T. Sfez, M. Quaglio, D. Brunazzo, L. Dominici, F. Michelotti, H. P. Herzig, O. J. F. Martin, and F. Giorgis, "Guided Bloch surface waves on ultrathin polymeric ridges," Nano Lett. **10**, 2087–2091 (2010).
35. K. R. Safronov, D. N. Gulkin, I. M. Antropov, K. A. Abrashitova, V. O. Bessonov, and A. A. Fedyanin, "Multimode interference of Bloch surface electromagnetic waves," ACS Nano **14**, 10428–10437 (2020).
36. R. Badugu, K. Nowaczyk, E. Descrovi, and J. R. Lakowicz, "Radiative decay engineering 6: fluorescence on one-dimensional photonic crystals," Anal. Biochem. **442**, 83–96 (2013).
37. I. V. Soboleva, V. V. Moskalenko, and A. A. Fedyanin, "Giant Goos-Hanchen effect and Fano resonance at photonic crystal surfaces," Phys. Rev. Lett. **108**, 123901 (2012).
38. F. Barachati, A. Fieramosca, S. Hafezian, J. Gu, B. Chakraborty, D. Ballarini, L. Martinu, V. Menon, D. Sanvitto, and S. Kéna-Cohen, "Interacting polariton fluids in a monolayer of tungsten disulfide," Nat. Nanotechnol. **13**, 906–909 (2018).
39. K. J. Moh, X. C. Yuan, J. Bu, S. W. Zhu, and B. Z. Gao, "Radial polarization induced surface plasmon virtual probe for two-photon fluorescence microscopy," Opt. Lett. **34**, 971–973 (2009).
40. C. J. Min, Z. Shen, J. F. Shen, Y. Q. Zhang, H. Fang, G. H. Yuan, L. P. Du, S. W. Zhu, T. Lei, and X. C. Yuan, "Focused plasmonic trapping of metallic particles," Nat. Commun. **4**, 2891 (2013).
41. J. N. Reddy, "On the numerical-solution of differential-equations by the finite-element method. 1. An introduction to the finite-element method — the Ritz models," Indian J. Pure Appl. Math. **16**, 1341–1376 (1985).
42. L. Lin, X. Peng, Z. Mao, X. Wei, C. Xie, and Y. Zheng, "Interfacial-entropy-driven thermophoretic tweezers," Lab Chip **17**, 3061–3070 (2017).
43. J. O'm. Bockris, M. A. V. Devanathan, and K. Müller, "On the structure of charged interfaces," Proc. R. Soc. London A **274**, 55–79 (1963).
44. A. Caciagli, R. Singh, D. Joshi, R. Adhikari, and E. Eiser, "Controlled optofluidic crystallization of colloids tethered at interfaces," Phys. Rev. Lett. **125**, 068001 (2020).
45. Y. Kuai, J. X. Chen, X. Tang, Y. F. Xiang, F. Y. Lu, C. F. Kuang, L. Xu, W. D. Shen, J. J. Cheng, H. Q. Gui, G. Zou, P. Wang, H. Ming, J. G. Liu, X. Liu, J. R. Lakowicz, and D. G. Zhang, "Label-free surface-sensitive photonic microscopy with high spatial resolution using azimuthal rotation illumination," Sci. Adv. **5**, eaav5335 (2019).
46. X. Zhao, Z. Yu, and T. Ding, "Quorum-sensing regulation of antimicrobial resistance in bacteria," Microorganisms **8**, 425 (2020).
47. K. Toma, E. Descrovi, M. Toma, M. Ballarini, P. Mandracci, F. Giorgis, A. Mateescu, U. Jonas, W. Knoll, and J. Dostálek, "Bloch surface wave-enhanced fluorescence biosensor," Biosens. Bioelectron. **43**, 108–114 (2013).
48. A. Farmer, A. C. Friedli, S. M. Wright, and W. M. Robertson, "Biosensing using surface electromagnetic waves in photonic band gap multilayers," Sens. Actuators B **173**, 79–84 (2012).
49. A. Sinibaldi, N. Danz, E. Descrovi, P. Munzert, U. Schulz, F. Sonntag, L. Dominici, and F. Michelotti, "Direct comparison of the performance of Bloch surface wave and surface plasmon polariton sensors," Sens. Actuators B **174**, 292–298 (2012).